Climatology, seasonality, and trends of oceanic coherent eddies

Josué Martínez-Moreno[1], Andrew McC. Hogg[1], and Matthew H. England[2]

[1]Research School of Earth Science and ARC Center of Excellence for Climate Extremes, Australian National University, Canberra, Australia

[2]Climate Change Research Centre (CCRC), UNSW Australia, Sydney NSW, Australia

Key Points:

- Kinetic energy of coherent eddies contain around 50% of the surface ocean kinetic energy budget.
- Seasonal cycle of the number of coherent eddies and coherent eddy amplitude reveal a 3-6 month lag to wind forcing
- Inverse cascade sets up the seasonal lag of the number and amplitude of coherent eddies.

Corresponding author: Josué Martínez-Moreno, `josue.martinezmoreno@anu.edu.au`

Abstract

Ocean eddies influence regional and global climate through mixing and transport of heat and properties. One of the most recognizable and ubiquitous feature of oceanic eddies are vortices with spatial scales of tens to hundreds of kilometers, frequently referred as "mesoscale eddies" or "coherent eddies". Coherent eddies are known to transport properties across the ocean and to locally affect near-surface wind, cloud properties and rainfall patterns. Although coherent eddies are ubiquitous, yet their climatology, seasonality and long-term temporal evolution remains poorly understood. Thus, we examine the kinetic energy contained by coherent eddies and we present the annual and long-term changes of automatically identified coherent eddies from satellite observations from 1993 to 2019. Around 50% of the kinetic energy contained by ocean eddies corresponds to coherent eddies. Additionally, a strong hemispherical seasonal cycle is observed, with a 3–6 months lag between the wind forcing and the response of the coherent eddy field. Furthermore, the seasonality of the number of coherent eddies and their amplitude reveals that the number of coherent eddies responds faster to the forcing ($\sim$3 months), than the coherent eddy amplitude (which is lagged by $\sim$6 months). Our analysis highlights the relative importance of the coherent eddy field in the ocean kinetic energy budget, implies a strong response of the eddy number and eddy amplitude to forcing at different time-scales, and showcases the seasonality, and multidecadal trends of coherent eddy properties.

Plain language summary

Coherent eddies are the most common feature in the oceans observable from satellites. They are crucial in ocean dynamics as they can transport properties over long distances and interact with the atmosphere. Our study investigates the seasonal and long-term changes in the abundance and intensity of coherent eddies, by automatically identifying individual eddies over the satellite altimeter record. The seasonal cycle suggests a transition from numerous, smaller, and weaker coherent eddies, to fewer and larger, and stronger coherent eddies over the season. In addition, a long-term adjustment of the coherent eddy field is identified possible due to long-term changes in the climate system.

1 Introduction

Mesoscale ocean variability with spatial scales of tens to hundreds of kilometers is comprised of processes such as vortices, waves, and jets (Ferrari & Wunsch, 2009; Fu et al., 2010). These mesoscale processes are highly energetic, and they play a crucial role in the transport of heat, salt, momentum, and other tracers through the ocean (Wunsch & Ferrari, 2004; Wyrtki et al., 1976; Gill et al., 1974). Possibly, the most recognizable and abundant process observed from satellites is mesoscale vortices. Although mesoscale vortices are commonly referred to in literature as "mesoscale eddies", this term is also often used to describe the total mesoscale ocean variability (the time-varying component of the mesoscale flow), thus, here we will refer to mesoscale vortices as *coherent eddies*.

Coherent eddies are quasi-circular currents. According to their rotational direction, the sea surface height anomaly within a coherent eddy can have a negative or positive sea surface height anomaly (cold-core and warm-core coherent eddies, respectively). This characteristic sea surface height signature of coherent eddies has been utilized to automatically identify and track coherent eddies from satellite altimetry (Cui et al., 2020; Martínez-Moreno et al., 2019; Ashkezari et al., 2016; Faghmous et al., 2015; Chelton et al., 2007). Automated identification algorithms of coherent eddies have shown their ubiquity in the oceans, with a predominant influence at hotpots of eddy activity such as boundary extensions and the Antarctic Circumpolar Current. In these regions, Chelton et al. (2011) estimated that coherent eddies contribute around 40–50% of the mesoscale kinetic energy (Chelton et al., 2011) and thus a significant fraction of the total kinetic energy (Ferrari & Wunsch, 2009). Although this unique estimate showcases the importance of the mesoscale coherent eddy field, the energy contained by coherent eddies was estimated by extracting the geostrophic velocities within the detected coherent eddies, thus it is possible it may contain energy from other processes. Coherent eddies are not only abundant and may have a large proportion of the surface kinetic energy budget, but they are also essential to ocean dynamics as concluded by many previous studies (Patel et al., 2020; Schubert et al., 2019; Pilo et al., 2015; Frenger et al., 2015, 2013; Beron-Vera et al., 2013; Siegel et al., 2011; Hogg & Blundell, 2006).

There is broad consensus that mesoscale eddy kinetic energy has a pronounced seasonal variability (Uchida et al., 2017; Kang & Curchitser, 2017; Qiu & Chen, 2004; Qiu, 1999). Several hypotheses have been proposed to explain this seasonality including: seasonal variations of atmospheric forcing (Sasaki et al., 2014), seasonality of the mixed layer depth (Qiu et al., 2014; Callies et al., 2015), seasonality of the intensity of barotropic instability (Qiu & Chen, 2004), the variability of the baroclinic instability due to the seasonality of the vertical shear (Qiu, 1999), and a seasonal lag of the inverse energy cascade (i.e. energy is transported between scales, from small to large; Arbic et al., 2013) in combination with the presence of a front in the mixed layer, which can lead to a seasonal cycle of the baroclinic instability (Qiu et al., 2014). On one hand, processes such as barotropic and baroclinic instabilities control the seasonality of coherent eddies in the ocean. On the other hand, recent studies using observations and eddy-permitting climate models suggest several long-term adjustments of the global ocean capable of long-term changes in the coherent eddy field. Such readjustments include a multidecadal increase in the ocean stratification resulted from temperature and salinity changes (Li et al., 2020), a horizontal readjusment of the sea surface temperature gradients (Ruela et al., 2020; Bouali et al., 2017; Cane et al., 1997), and an intensification of the kinetic energy, eddy kinetic energy, and mesoscale eddy kinetic energy over the last 3 decades as a consequence of an increase in wind forcing (Hu et al., 2020; Wunsch, 2020; Martínez-Moreno et al., 2021). All these seasonal factors and long-term readjustments directly influence the annual and decadal response of the coherent eddy field, however, the seasonality of the coherent component of the eddy kinetic energy, as well as the seasonal cycle and trends of the coherent eddy statistics remain unknown.

Here we present a new global climatology of the coherent eddy kinetic energy by reconstructing the coherent eddy signature from satellite observations. Our study documents the seasonal cycle of the coherent eddy kinetic energy, and seasonal cycle and long-term trends of the coherent eddy properties over the satellite record. Moreover, we conduct more detail analysis in regions where coherent eddies dominate the eddy kinetic energy field. This paper is structured as follows: the data sources and methodology are described in section 2. Then, we present the climatology, energy ratios, and global seasonality of the coherent eddy kinetic energy in section 3. Section 4 presents the global climatology and seasonality of coherent eddy properties, followed by long-term changes of the coherent eddy properties (section 5). Then we focus our attention on the seasonal cycle and coherent eddy properties in regions dominated by coherent eddies (section 6). Finally, section 7 summarizes the main results and discusses the implications of this study.

2 Methods

We use daily sea surface height (SSH) data made available by the Copernicus Marine Environment Monitoring Service in near real time (CMEMS, 2017). This gridded product contains the sea surface height and geostrophic velocities with daily 0.25° resolution from January 1993 to 2019. The daily geostrophic velocities allowed us to compute the kinetic energy (KE) and eddy kinetic energy (EKE) over the satellite record. The main source of EKE is the time-varying wind (Ferrari & Wunsch, 2009), thus we computed the seasonal cycle of the wind magnitude from the JRA55 reanalysis (Japan Meteorological Agency, Japan, 2013) using wind velocities at 10m above the ocean's surface.

Over the same record, coherent eddy statistics from Martínez-Moreno et al. (2019), hereafter M-M, are analyzed and compared to those released by Chelton & Schlax (2013), both datasets are gridded in a 1° resolution. Although both datasets are produced via automated eddy identification algorithms using closed contours of SSH, these datasets have important differences in the criteria they use to identify and record coherent eddies statistics. The major differences include; (i) M-M's algorithm requires an adjustment between a 2D Gaussian and the SSH anomaly (SSHa) surface within the identify closed contour, while Chelton's only uses the outer-most closed contour of SSH; (ii) M-M's dataset reports the maximum SSHa within the identified coherent eddy, while Chelton's algorithm reports the maximum SSH value minus the discrete level in which the coherent eddy was identified; M-M's dataset includes all detected coherent eddies, while Chelton's dataset excludes (iii) coherent eddies with lifetimes shorter than four weeks and (iv) coherent eddy amplitudes smaller than 1cm. Moreover, M-M's algorithm allows the reconstruction of the coherent eddy field under the assumption that coherent eddies have a 2D Gaussian imprint in the sea surface height. This Gaussian reconstruction of the coherent eddy field then allow us to estimate the coherent geostrophic eddy velocities and thus the kinetic energy contained only by coherent eddies.

2.1 Kinetic Energy decomposition

Kinetic energy is commonly divided into the mean and time-varying components through a Reynolds decomposition. At a given time, the surface velocity field $\mathbf{u} = (u, v)$ is split into the time mean ($\overline{\mathbf{u}}$) and time varying components ($\mathbf{u}'$). Moreover, M-M proposed to further decompose the eddy kinetic energy into the energy contained by coherent features ($\mathbf{u'_e}$) and non-coherent features ($\mathbf{u'_n}$). Therefore the KE equation can be written as:

$$\mathrm{KE} = \underbrace{\overline{u}^2 + \overline{v}^2}_{\text{MKE}} + \underbrace{\underbrace{{u'}_e^2 + {v'}_e^2}_{\text{CEKE}} + \underbrace{{u'}_n^2 + {v'}_n^2}_{\text{nCEKE}} + \mathcal{O}_c^2}_{\text{EKE}} + \mathcal{O}^2 \tag{1}$$

Due to the properties of this decomposition, the second order term $\mathcal{O}^2$ is zero when averaged over the same period as $\overline{\mathbf{u}}$. However, $\mathcal{O}_c^2$ is not necessarly negligible, unless it is averaged over time and space. More information about the decomposition of the field into coherent features and non-coherent features is explained by Martínez-Moreno et al. (2019). A global snapshot of each component of kinetic energy decomposition is shown in Figure 1, where the KE and EKE are comprised of rings and filaments. As expected, the decomposition of EKE into CEKE and nCEKE components exhibit only ring-like signatures expected of coherent eddies, while the non-coherent component shows filaments and some miss-identified coherent eddies.

2.2 Eddy statistics

The eddy statistics used in this study include (i) the eddy count (cEddy_n) defined as the number of eddies per grid cell, (ii) the eddy diameter defined as the diameter of a circle with equal area as the closed contour of each identified eddy, and (iii) the mean eddy amplitude defined as the mean amplitude of the coherent eddies within the cell (cEddy_{amp}). The latter metric can be separated into positive (cEddy^+_{amp}) and negative (cEddy^-_{amp}) coherent eddy amplitudes, defined as the mean amplitude of warm core and cold core coherent eddies, respectively, within the cell. The polarity independent eddy amplitude ($|\mathrm{cEddy}_{amp}|$) is defined as:

$$|\mathrm{cEddy}_{amp}| = \frac{1}{2}\left(\mathrm{cEddy}^+_{amp} - \mathrm{cEddy}^-_{amp}\right) \tag{2}$$

Note that the cEddy^+_{amp} and cEddy^-_{amp} are sign definite, thus the difference will always be positive, the gridded averaged cEddy_{amp} can be negative or positive noting the dominant polarity of coherent eddies in the region, and the absolute cEddy_{amp} is denoted by $\mathrm{cEddy}_{|amp|}$. We analyze the climatology, seasonal cycles and trends of the eddy statistics between 1993 and 2019. We exclude the equatorial region (10°S - 10°N) and pole-

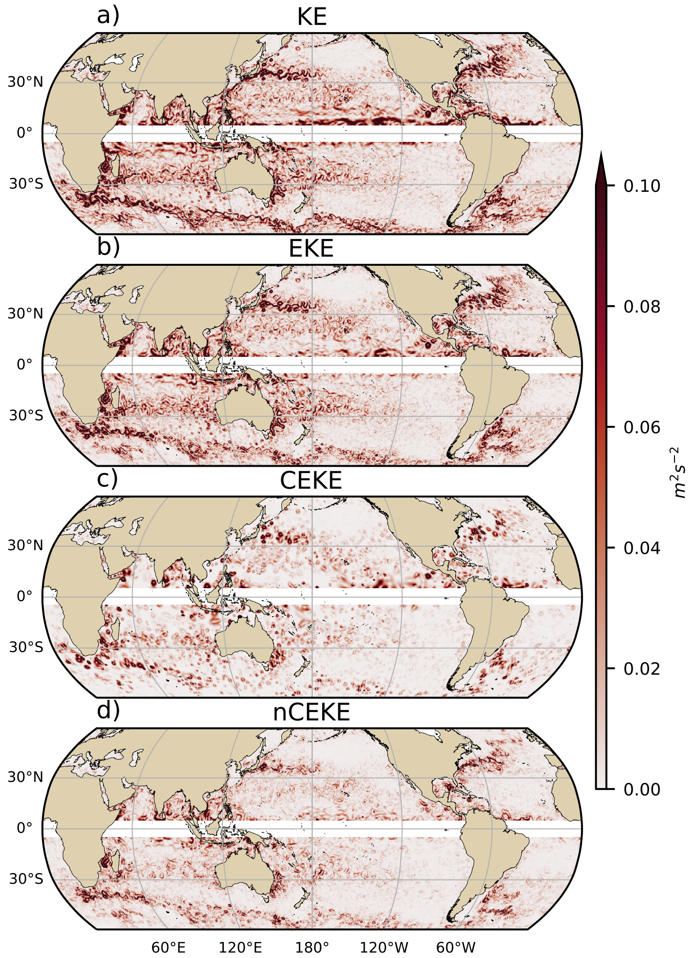

Figure 1. Snapshot of surface kinetic energy ($\overline{\mathrm{KE}}$), surface eddy kinetic energy ($\overline{\mathrm{EKE}}$), surface coherent eddy kinetic energy ($\overline{\mathrm{CEKE}}$), and surface non-coherent eddy kinetic energy ($\overline{\mathrm{nCEKE}}$) for the 1st of January 2017.

ward of 60°. Note that the climatology of cEddy$_n$ is computed by adding all the identified eddies over the record, while all other climatological statistics are computed as the time-average over the record. Seasonal climatologies are calculated for the monthly average of each coherent eddy statistic, while hemispherical time-series are filtered with a running average of 90 days. Trends of cEddy$_n$ and $|$cEddy$_{amp}|$ are calculated by coarsening the dataset to a 5° grid, and then linear trends are computed for each grid point, the statistical significance is assessed by a modified Mann-Kendall test (Yue & Wang, 2004).

Time averages are denoted by $\overline{}$, while area-weighted averages are denoted using $\langle\ \rangle$, the area weighted of function f is:

$$\langle f \rangle = \frac{\int f dxdy}{\int dxdy}, \tag{3}$$

area-weighted coherent eddy properties masked areas each time, where no coherent eddies were identified.

3 Global Coherent Eddy Energetics

The kinetic energy decomposition estimated from sea surface height measured by satellite altimeters is shown in Figure 2. These maps show that many regions of the global ocean are highly energetic in mean KE ($\overline{\mathrm{KE}}$), mean EKE ($\overline{\mathrm{EKE}}$), mean coherent eddy kinetic energy ($\overline{\mathrm{CEKE}}$) and mean non-coherent eddy kinetic energy ($\overline{\mathrm{nCEKE}}$). The spatial pattern highlights well known regions of the ocean where mesoscale processes are abundant, such as the western boundary extensions and the Antarctic Circumpolar Current. Remarkably, the spatial distribution of the energy contained by the reconstructed mesoscale coherent eddies and non-coherent components are similar (Figures 2c,d). However, there are some regions where coherent eddies dominate over non-coherent, and vice-versa. Overall, this decomposition suggest that boundary current extensions and other energetic regions, in particularly, eddy-rich regions in the ocean contain both coherent and non-coherent components of the kinetic energy.

Eddy kinetic energy is known to be more than an order of magnitude greater than MKE (Gill et al., 1974); this result is clearly shown in Figure 3a, where $\overline{\mathrm{EKE}}$ is responsible for almost all the $\overline{\mathrm{KE}}$ across the ocean, except for regions with persistent currents over time. Such regions are located in the mean boundary extension locations, the equatorial Pacific currents and regions in the Antarctic Circumpolar Current, where the $\overline{\mathrm{EKE}}$ explains around 40% of the $\overline{\mathrm{KE}}$. In a previous study, Chelton et al. (2011) estimated that the EKE within coherent eddies with lifetimes greater than 4 weeks contain between 40 to 60 percent of the $\overline{\mathrm{EKE}}$. Our method to reconstruct the coherent eddy signature (Figure 3b) further corroborates that the coherent component ($\langle\overline{\mathrm{CEKE}}\rangle$) has $\sim$48% of the $\langle\overline{\mathrm{KE}}\rangle$ (Figure 3d). Furthermore, global area averages of the ratios show $\langle\overline{\mathrm{EKE}}\rangle$ explains $\sim$78% of the ocean $\langle\overline{\mathrm{KE}}\rangle$ field, while non coherent eddy features contain $\sim$57% percent of the $\langle\overline{\mathrm{EKE}}\rangle$. Note the globally averaged coherent and non coherent components do not add to 100% as the cross terms ($\mathcal{O}_c^2$) are non-zero, due to coherent eddy reconstruction

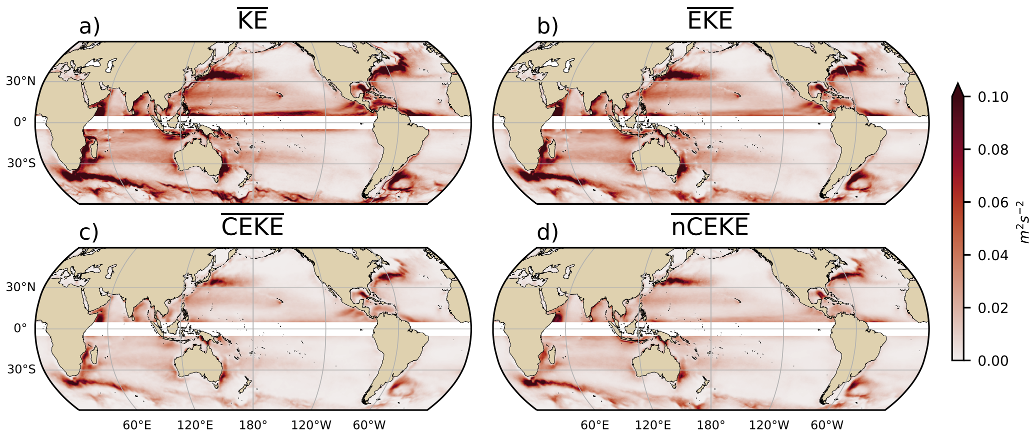

Figure 2. Mean surface kinetic energy ($\overline{\text{KE}}$), surface eddy kinetic energy ($\overline{\text{EKE}}$), surface coherent eddy kinetic energy ($\overline{\text{CEKE}}$), and surface non-coherent eddy kinetic energy ($\overline{\text{nCEKE}}$) between 1993-2018.

errors. The spatial pattern reveals a dominance of the $\overline{\text{CEKE}}$ equatorward from the boundary extensions and areas with large coherent eddy contributions of around 80% of the region's eddy kinetic energy can be found south of Australia, the Tehuantepec Gulf, and the tropical Atlantic. An evident signal is an reduction of the energy contained by coherent eddies at high latitudes and an increase in the energy explained by non-coherent eddies; this signal could be a consequence of the incapability of the 0.25° satellite resolution ($\sim$ 13 km at 60°) to resolve coherent eddies with scales smaller than $\sim$10 km (first baroclinic Rossby radius at 60°; Chelton et al. 1998).

Figure 4 shows the seasonal cycle of the area weighted EKE and CEKE for the Northern Hemisphere ($\langle\text{EKE}\rangle_{NH}$ and $\langle\text{CEKE}\rangle_{NH}$; 10°N - 60°N) and Southern Hemisphere ($\langle\text{EKE}\rangle_{SH}$ and $\langle\text{CEKE}\rangle_{SH}$; 60°S - 10°S). In both hemispheres, the $\langle\text{EKE}\rangle$ and $\langle\text{CEKE}\rangle$ peak during summer. In the Northern Hemisphere, the largest $\langle\text{EKE}\rangle_{NH}$ and $\langle\text{CEKE}\rangle_{NH}$ occurs in July, $\sim$6 months after the maximum winds in January (purple bar and back star in Figure 4c and d). Meanwhile, the Southern Ocean $\langle\text{EKE}\rangle_{SH}$ and $\langle\text{CEKE}\rangle_{SH}$ seasonal maxima arises during December, $\sim$4 months after the maximum winds in August (purple bar and back star in Figure 4g, and h). This lag between winds and the eddy and coherent eddy energy components is further discussed in section 4.

The cyclic plots in Figure 4 show the temporal evolution of $\langle\text{EKE}\rangle$ and $\langle\text{CEKE}\rangle$. Note that high frequency variability can be observed in the $\langle\text{CEKE}\rangle$ field with tempo-

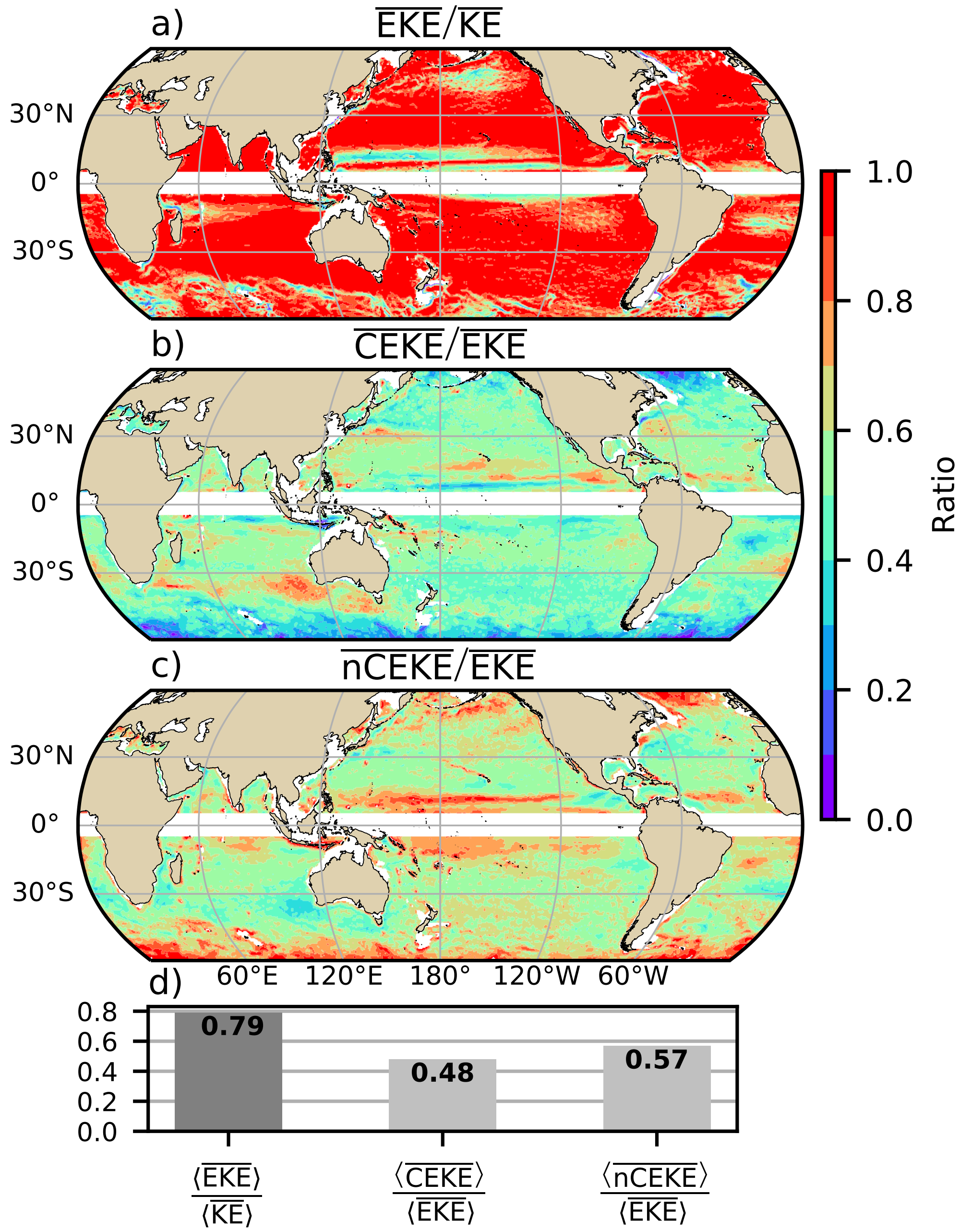

Figure 3. Ratios of the kinetic energy components. a) Map of the proportion of mean eddy kinetic energy ($\overline{\mathrm{EKE}}$) versus mean kinetic energy ($\overline{\mathrm{KE}}$); b) Map of the percentage of mean coherent eddy kinetic energy ($\overline{\mathrm{CEKE}}$) versus mean eddy kinetic energy ($\overline{\mathrm{EKE}}$); c) Map of the percentage of mean non-coherent eddy kinetic energy ($\overline{\mathrm{nCEKE}}$) versus mean eddy kinetic energy ($\overline{\mathrm{EKE}}$); d) Global time and area averaged (represented by $\langle\rangle$) percentage of mean eddy kinetic energy ($\langle\overline{\mathrm{EKE}}\rangle$) versus the global mean kinetic energy ($\langle\overline{\mathrm{KE}}\rangle$), area averaged percentage of mean coherent eddy kinetic energy ($\langle\overline{\mathrm{CEKE}}\rangle$) and mean non coherent eddy kinetic energy ($\langle\overline{\mathrm{nCEKE}}\rangle$) versus global mean eddy kinetic energy ($\langle\overline{\mathrm{EKE}}\rangle$). Regions where the depth of the ocean is shallower than 1000m are removed from the ratio estimation.

ral scales of a few months, this could be attributed local dynamics averaged over the hemisphere, as well as errors within the coherent eddy reconstruction. Additionally, concentric changes in the cyclic plots highlight long-term changes over the record. For example, the Northern Hemisphere winters in early years of the record (blue) had a more energetic coherent eddy field, which has transitioned to weaker coherent energy contents since 2010 (red), in other words, the intensity of the $\langle \text{CEKE} \rangle_{NH}$ field has decreased. A larger long-term change can be observed in the Southern Hemisphere, where concentric growth over time in $\langle \text{EKE} \rangle_{SH}$ and $\langle \text{CEKE} \rangle_{SH}$ support the previously observed strengthening of the eddy field in the Southern Ocean (Hogg et al., 2015; Martínez-Moreno et al., 2019; Martínez-Moreno et al., 2021).

4 Global Coherent Eddy Statistics

Coherent eddy kinetic energy allows us to quantify and study the energy of the eddy field, but the coherent eddy properties computed by automated coherent eddy identification algorithms allow us investigate in more detail the contribution and temporal changes of their abundance (the number of eddies) and their intensity (both their amplitude and diameter). Figure 5 shows gridded climatologies of the number of eddies and the eddy amplitude. We contrast our M-M eddy count with Chelton et al. (2007) (Figure 5a-b). Although the number of the identified eddies is larger in M-M, possibly due to the lifespan filter implemented by Chelton, both datasets reveal consistent spatial patterns. For example, both datasets show high abundance of eddies in the East North Pacific, East North Atlantic, as well as the East South Pacific, East South Atlantic and East Indian Ocean, and small number counts of eddies in the tropics and in high latitudes ($\sim 60°$). An interesting pattern also emerges in both eddy count datasets, where small scale structures with larger eddy counts are favored across the ocean. In addition, to preferential coherent eddy paths observable in boundary extensions and regions in the Southern Ocean. These clusters and paths of coherent eddies could be associated with topographic features, however they remain a puzzling consistency between the eddy count pattern using these two eddy identification methods.

Regions with large counts of eddies have in general small absolute amplitudes (Figure 5 c), ocean gyre interiors follow with a larger absolute amplitude and finally regions such as the boundary extensions and Antarctic Circumpolar Current have the largest coherent eddy absolute amplitudes as shown by Chelton et al. (2011). Eddy amplitude

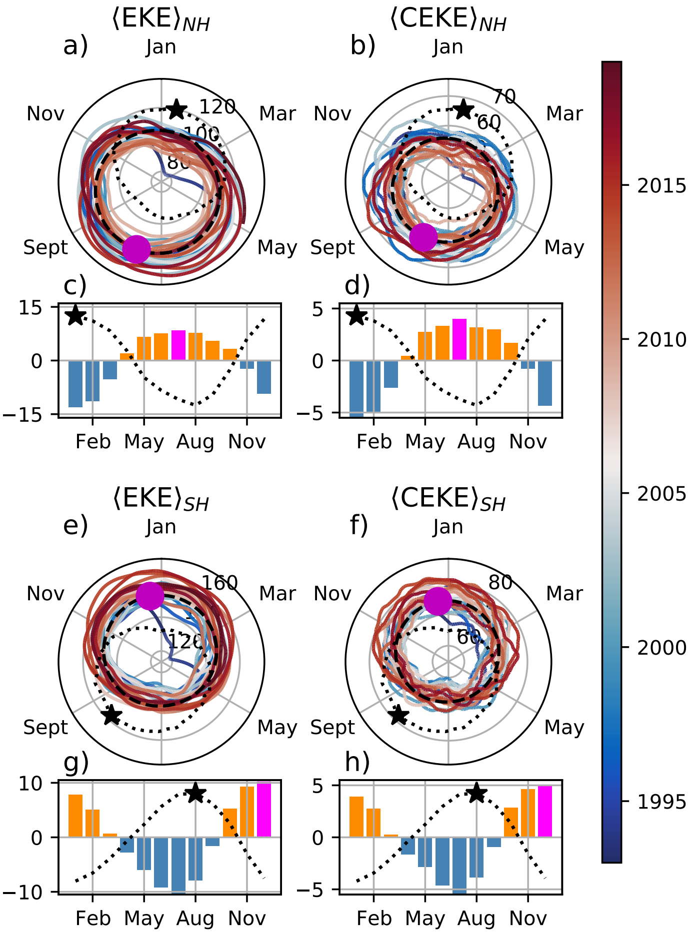

246 **Figure 4.** Seasonality of the area weighted eddy kinetic energy (⟨EKE⟩), coherent eddy ki-
247 netic energy (⟨CEKE⟩). Panels a and b show the time-series of the Northern Hemisphere, while
248 panels e and f correspond to the Southern Hemisphere. Panels c and d show the seasonal cycle of
249 the $\langle\text{EKE}\rangle_{NH}$ and $\langle\text{CEKE}\rangle_{NH}$ in the Northern Hemisphere, and panels g and h show the South-
250 ern Hemisphere ($\langle\text{EKE}\rangle_{SH}$ and $\langle\text{CEKE}\rangle_{SH}$). Dashed lines correspond to the seasonal cycle of the
251 fields and dotted lines show the seasonal cycle of the wind magnitude smoothed over 120 days
252 (moving average). The black and magenta markers (circle and bar) show the maximum of the
253 seasonal cycle for the kinetic energy components and the wind magnitude, respectively. In cyclic
254 plots, line colors shows the year.

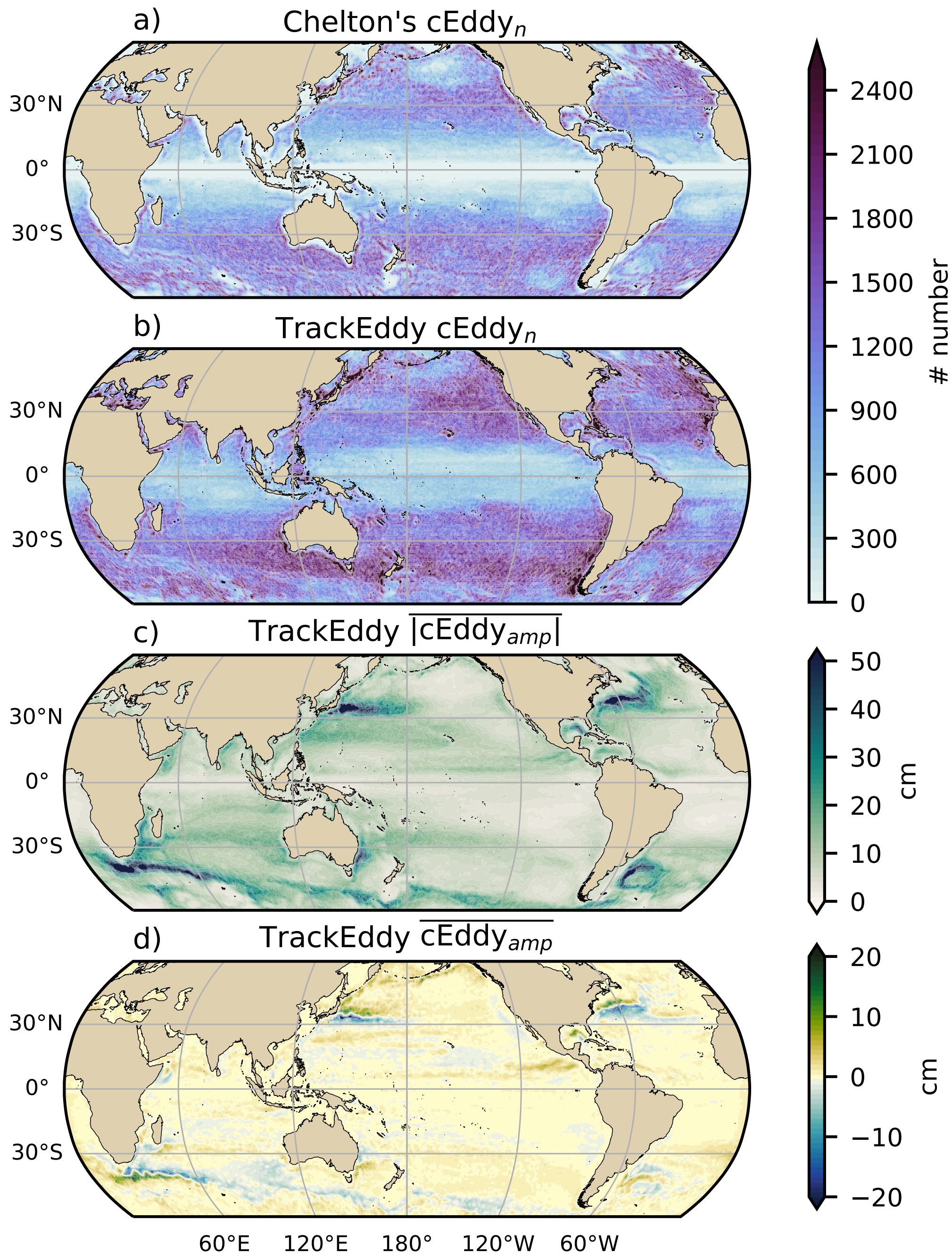

Figure 5. Averaged coherent eddy statistics. a) Climatology of the number of coherent eddies (cEddy$_n$) identified by Chelton et al. (2007); b) Climatology of the number of coherent eddies (cEddy$_n$) identified by Martínez-Moreno et al. (2019); c) Climatology of the mean absolute coherent eddy amplitude (cEddy$_{amp}$). d) Climatology of the mean coherent eddy amplitude (cEddy$_{amp}$).

highlights regions dominated by a given coherent eddy polarity, for example, boundary extensions have a preferred sign (Figure 5 d); positive amplitude polewards of the boundary extension mean location, and negative amplitude equatorwards. This sign preference is consistent with the preferential way coherent eddies are shed from boundary extensions; warm core eddies (positive) polewards of the boundary current extension, and equatorward for cold core eddies (negative) (Kang & Curchitser, 2013; Chelton et al., 2011, 2007). These global statistics reveal the absolute coherent eddy amplitude is a proxy of the CEKE with similar spatial patterns (Figure 2 & Figure 5 c) and showcases that regions where $\overline{\text{CEKE}}$ has a large proportion of $\overline{\text{EKE}}$ (Figure 3), the absolute coherent eddy amplitude is also large.

To further understand the seasonal cycle of $\langle\text{CEKE}\rangle$, we compute the climatology of coherent eddy properties in each hemisphere (Figure 6). The seasonality of the number of eddies in the Northern Hemisphere peaks on April (Figure 6 a, c), while the Southern Hemisphere maximum number of eddies occurs during October (Figure 6 e, g). Meanwhile, the seasonality of the polarity independent eddy amplitude ($\left\langle|\text{cEddy}_{amp}|\right\rangle$) peaks in August and January for the Northern and Southern Hemispheres respectively (Figure 6 b, d, f, and h). As expected, the seasonality of $\left\langle|\text{cEddy}_{amp}|\right\rangle$xw, or equivalent to the intensity of the coherent eddies, is consistent with the seasonal cycle of $\langle\text{CEKE}\rangle$. Furthermore, a distinct lag of $\sim$3 months is observed between the winds and eddy count, while the eddy amplitude maximum occurs $\sim$6 months after the seasonal maxima in winds. We observe the eddy number increases earlier in the year and through eddy-eddy interactions (merging of coherent eddies) the amplitude of the coherent eddy increases $\sim$3 months after. This seasonal lag and summer maxima is consistent with Figure 5, furthermore, previous studies suggest that a time-lag of the inverse cascade (Sasaki et al., 2014; Qiu et al., 2014) is responsible of the EKE seasonal cycle, where winter has the highest energy at the smallest scales (non-resolvable with satellite observations), spring and autumn have the highest and lowest energy in scales of 50-100 km, and summertime has the highest energy at the largest scales ($>$ 100 km; Uchida et al. 2017). Thus, the maximum of $\langle\text{EKE}\rangle$, $\langle\text{CEKE}\rangle$, and $\left\langle|\text{cEddy}_{amp}|\right\rangle$ located during summertime suggest that the seasonality of eddies and coherent eddies could be dominated by scales larger than 100 km. This result can be further explored by looking at the seasonal evolution of the eddy diameter (cEddy_d). Note that 90% of identified coherent eddies have diameters between 50 to 220 km (Figure 7 a). We divided eddies into large-scale coherent eddies (diameter > 120 km) and small-scale coherent eddies (diameter < 120 km; Figure 7a). In the Northern Hemisphere, small eddies have a seasonal peak in diameter during May, while large eddies have the greatest diameter in September (Figure 7 b). Meanwhile, in the Southern Hemisphere, the small-scale coherent eddies have the maximum diameter in December, while large-scale coherent eddies peak in February (Figure 7 c). This result suggests that wind driven baroclinic instabilities generate small coherent eddies early in the season, which then merge and grow to become larger in diameter and amplitude, and thus, more energetic. This process is associated with the inverse energy cascade, and suggest that this mechanism not only drives the EKE seasonality, but also may be responsible of the seasonal cycle of coherent eddies.

Long-term changes can be observed in Figure 6a,b, e, and f where growing-shrinking concentric circles over time denote an increase-decrease trend of the field. This trend is particularly evident in the Southern Hemisphere, where the number of eddies has decreased, the eddy amplitude has increased. This result is consistent with the observed trends in EKE and mesoscale EKE in the Southern Ocean (Hogg et al., 2015; Martínez-Moreno et al., 2019).

Seasonality of the area weighted eddy kinetic energy ($\langle \text{EKE} \rangle$), coherent eddy kinetic energy ($\langle \text{CEKE} \rangle$). Panels a and b show the time-series of the Northern Hemisphere, while panels e and f correspond to the Southern Hemisphere. Panels c and d show the seasonal cycle of the $\langle \text{EKE} \rangle_{NH}$ and $\langle \text{CEKE} \rangle_{NH}$ in the Northern Hemisphere, and panels g and h show the Southern Hemisphere ($\langle \text{EKE} \rangle_{SH}$ and $\langle \text{CEKE} \rangle_{SH}$). Dashed lines correspond to the seasonal cycle of the fields and dotted lines show the seasonal cycle of the wind magnitude smoothed over 120 days (moving average). The black and magenta markers (circle and bar) show the maximum of the seasonal cycle for the kinetic energy components and the wind magnitude, respectively. In cyclic plots, line colors shows the year.

The coherent eddy amplitude from positive coherent eddies and negative coherent eddies show similar seasonal cycles to the absolute eddy amplitude. The Northern Hemisphere decrease in absolute eddy amplitude is driven by a decrease of the amplitude of negative coherent eddies in the Northern Hemisphere. Meanwhile in the Southern Ocean, the increase in absolute eddy amplitude is corroborated by an strengthening of both coherent eddy polarities since the early 90s.

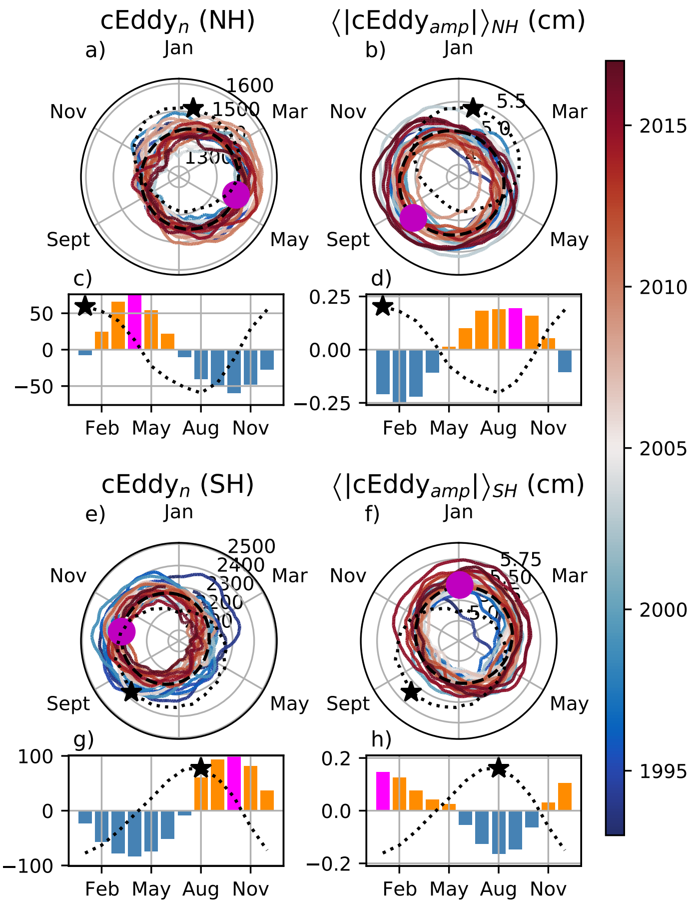

Figure 6. Seasonality of the count of number of eddies (cEddy$_n$) and area weighted polarity independent coherent eddy amplitude ($\langle$cEddy$_{amp}\rangle$); Panels a and b show the time-series of the Northern Hemisphere, while panels e and f correspond to the Southern Hemisphere. Panels c and d show the seasonal cycle of the cEddy$_n$ and $\langle|\text{cEddy}|_{amp}\rangle_{NH}$ in the Northern Hemisphere, and panels g and h show the Southern Hemisphere (cEddy$_n$ and $\langle|\text{cEddy}|_{amp}\rangle_{SH}$). Dashed lines correspond to the seasonal cycle of the fields and dotted lines show the seasonal cycle of the wind magnitude smoothed over 120 days (moving average). The black and magenta markers (circle and bar) show the maximum of the seasonal cycle for the eddy property and the wind magnitude, respectively. In cyclic plots, line colors shows the year.

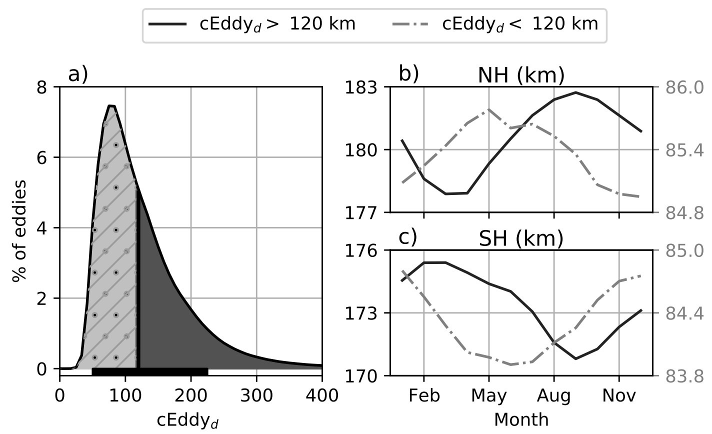

Figure 7. Distribution of the identified eddy diameter (cEddy$_d$; km) and hemispherical seasonality of the coherent eddy diameter. a) Distribution in percentage of identified eddy amplitude, solid bar bellow distribution represents 90% of the identified eddies. Seasonal cycle of the eddy diameter for the b) Northern Hemisphere and c) Southern Hemisphere. Dark solid line and area corresponds to coherent eddies with diameters larger than 120 km, while light gray dash-dotted line and area shows coherent eddies with diameters smaller than 120 km.

5 Trends

The results presented in Figures 4 and 6 suggest a long-term readjustment of the coherent eddy field. The long-term trends of the number of coherent eddies, absolute coherent eddy amplitude, and coherent eddy amplitude polarities are explored in Figure 8. Chelton's and M-M datasets show consistent spatial patterns in the trends and significance of the number of coherent eddies and the absolute coherent eddy amplitude. Several regions in the ocean, such as the Southern Ocean, North Atlantic and North Pacific, show a decrease in the number of eddies. Those same regions also have a clear increase in the absolute coherent eddy amplitude. These trends are similar to those observed in mesoscale eddy kinetic energy (Martínez-Moreno et al., 2021) and provide additional evidence of a readjustment of the mesoscale eddy field over the last 3 decades.

@Matt: *What do you think? Is it important to highlight the trends we observe are different to sea level rise? Or is the next paragraph irrelevant?*

The observed trends of cEddy$_{|amp|}$ in several oceanic regions have the same scale as sea level rise (~3cm per decade) by analyzing the positive and negative coherent eddy

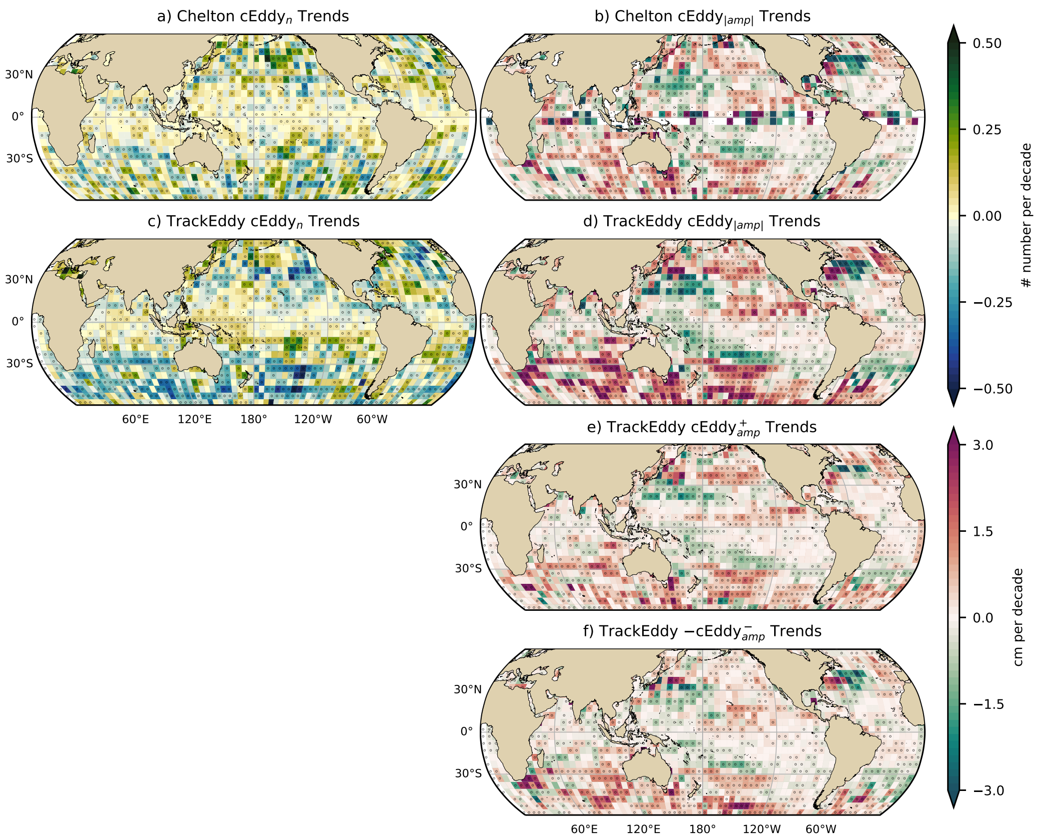

Figure 8. Trends of coherent eddy statistics. a) and b) Trends of the number of identified coherent eddies from satellite observations identified using TrackEddy, and those reported in Chelton's dataset. c) and d) Trends of the absolute value of identified coherent eddies amplitude (cEddy$_{|amp|}$) from satellite observations identified using TrackEddy, and those reported in Chelton's dataset. e) and f) Trends of eddy amplitude polarity using TrackEddy (cEddy$^+_{amp}$ and cEddy$^-_{amp}$). Gray stippling shows regions that are statistically significant above the 95% confidence level.

amplitude we can discard the observed trends correspond to an increase in sea level. In fact, each coherent eddy polarity has intensified in the Southern Ocean and North East Pacific and Atlantic. In other words, the amplitude of each polarity has increased over time, thus this strengthening is an intrinsic response of the coherent eddy field. Note that the negative coherent eddy amplitude dominates the global |cEddy$_{amp}$| trends (Figure 8e, f). However, different trend pattern can be observed in both positive and negative coherent eddy amplitudes in the north Atlantic and north Pacific, where the negative coherent eddy amplitude in the Western Boundary Currents appears to decrease.

6 Regional Climatology

For regions with relatively large proportions of CEKE located at boundary extensions and eastern currents, we investigate the seasonal and long-term variability of the coherent eddy properties.

The most energetic western boundary extensions include; the Gulf Stream, the Kuroshio Current, and the Agulhas Current (Figures 9, 10, and 11). Coherent eddy generation in boundary extensions occurs through baroclinic and barotropic instabilities of the mean current, thus all these regions share similar generation dynamics. In all these regions without exception; (i) CEKE contains up to 80% of the EKE in regions equatorwards from the mean western boundary extension location, (ii) the number of eddies is consistently minimal numbers of eddies over the mean western boundary extension location, and (iii) the eddy amplitude is larger polewards of the mean western boundary extension location.

In the Gulf Stream, the energy ratio between CEKE and EKE is ∼56% (Figure 9). The highest energy content occurs in regions with numerous eddies, and collocated with regions where the largest $|\text{cEddy}_{amp}|$ gradients occurs. The time series of cEddy_n and $\langle|\text{cEddy}_{amp}|\rangle$ are anti-correlated (-0.52), and they display inter-annual and seasonal variability. Although Chaudhuri et al. (2009) observed a positive phase of North Atlantic Oscillation (NAO) exhibit higher EKE, due to an increase in baroclinic instabilities, thus suggesting more coherent eddies, we do not find a correlation between the cEddy_n or the $\langle|\text{cEddy}_{amp}|\rangle$ in the Gulf Stream and the NAO index. Similar to the signal observed in the hemispherical analysis, the eddy count seasonal cycle follows the wind maximum after ∼3 months, while the amplitude of the coherent eddies lags by ∼ 6 months.

The variability of the cEddy_n and $\langle|\text{cEddy}_{amp}|\rangle$ in the Kuroshio Current are weakly anti-correlated (-0.41; Figure 10). However, on average 56% of the energy in the region corresponds to CEKE. As observed in the Gulf Stream, there is an important seasonal cycle in the boundary extensions, where the eddy count seasonal cycle occurs on March after ∼3 months of the wind maximum (January). Meanwhile, the amplitude of the coherent eddies lags by ∼ 6 months (June) after the maximum wind.

In the Southern Hemisphere, the strongest boundary current, the Agulhas Current shows similar behavior to its counterparts in the Northern Hemisphere (Figure 11). On

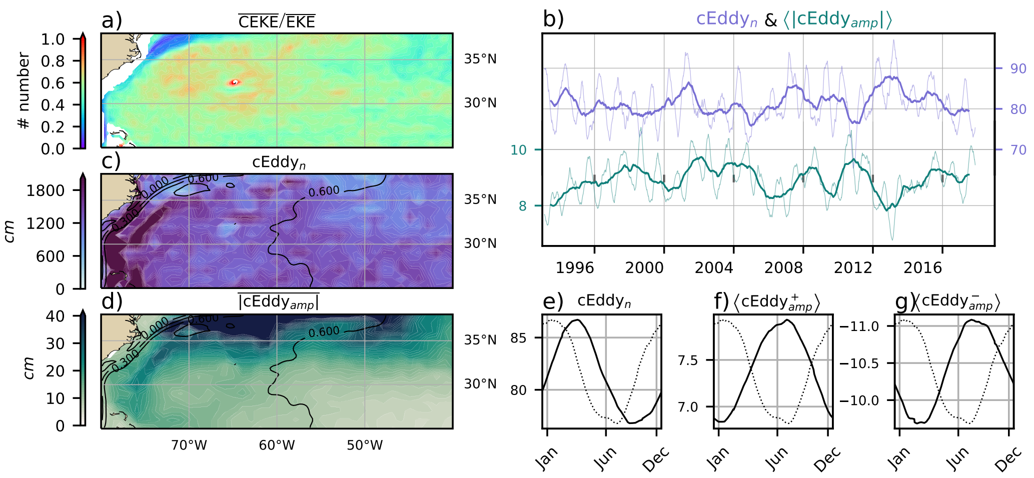

Figure 9. Climatology of the eddy field and coherent eddy field at the Gulf Stream. a) Ratio of mean coherent eddy kinetic energy ($\overline{\mathrm{CEKE}}$) versus mean eddy kinetic energy ($\overline{\mathrm{EKE}}$); b) Thick lines show the running average over 2 years and thin lines show the running average over 90 days of the coherent eddy number sum and the average coherent eddy amplitude; c) Map of the number of eddies; d) Map of the average coherent eddy amplitude; e) Seasonal cycle of the number of eddies f) Seasonal cycle of the positive coherent eddy amplitude. g) Seasonal cycle of the negative coherent eddy amplitude. Contours in maps correspond to mean sea surface height (m).

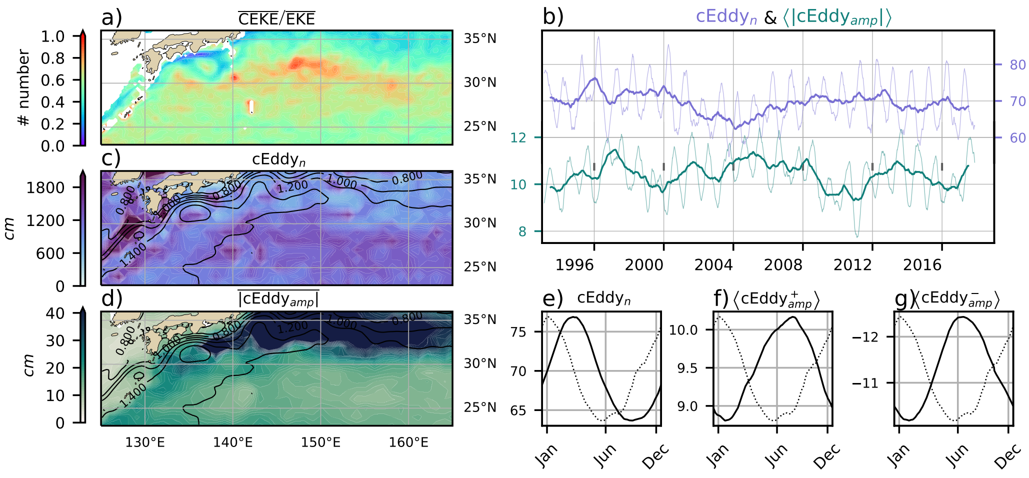

Figure 10. Climatology of the eddy field and coherent eddy field at the Kuroshio extension. a) Ratio of mean coherent eddy kinetic energy ($\overline{\text{CEKE}}$) versus mean eddy kinetic energy ($\overline{\text{EKE}}$); b) Time-series of the coherent eddy number and the average coherent eddy amplitude; c) Map of the number of eddies; d) Map of the average coherent eddy amplitude; Seasonal cycle of the e) number of eddies, f) positive coherent eddy amplitude, and g) negative coherent eddy amplitude. Different lines represent the same as in Figure 9.

average, coherent eddies in the Agulhas current contain ∼56% of the energy, meanwhile the cEddy$_n$ seasonal peak occurs in August, while the $\langle|\text{cEddy}_{amp}|\rangle$ occurs in January-February. The seasonal lag between the winds, eddy count, and eddy amplitude in each of the western boundary current extensions is interpreted as being analogous to the explanation observed in Figure 6 of the lagged response of coherent eddy properties due to eddy-eddy interactions, consistent with the inverse cascade of energy.

Coherent eddies dominate the EKE field in other regions such as the Leeuwin Current (Figure 12), where the 65% of the energy is contained by coherent eddies. Although the Leeuwin region is not characterized by having a large EKE, however, a considerable abundance of eddies and large eddy amplitudes are observable in the region. The series reveal a significant increase in the $\langle|\text{cEddy}_{amp}|\rangle$, while the cEddy$_n$ has decreased over the last 3 decades ()**@Andy**, you suggested a reference here, I couldn't find it.... The seasonal cycle shows that the cEddy$_n$ peak occurs on August, 3 months after the maximum winds (June). Meanwhile, the $\langle\text{cEddy}^+_{amp}\rangle$ responds in synchrony to winds, and the $\langle\text{cEddy}^-_{amp}\rangle$ is in phase with the seasonal cycle of the cEddy$_n$.

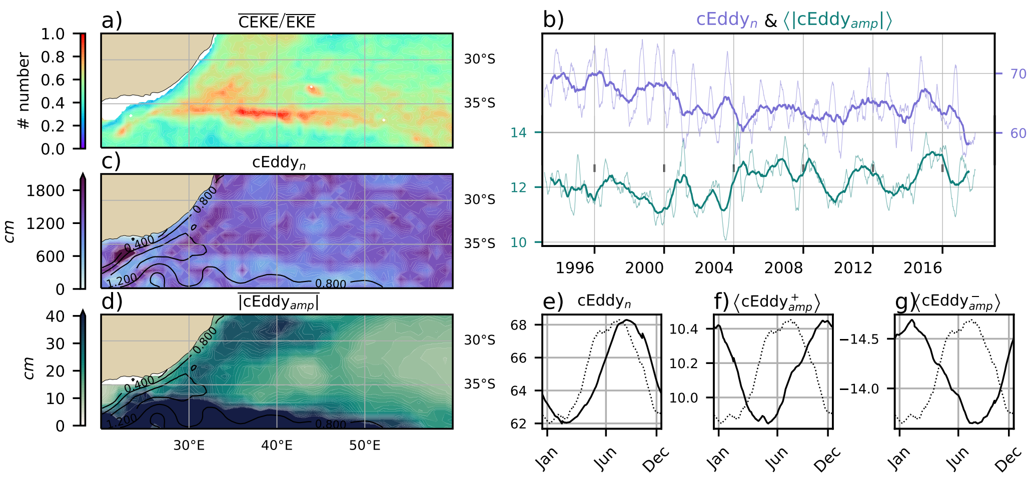

Figure 11. Climatology of the eddy field and coherent eddy field at the Agulhas Current. a) Ratio of mean coherent eddy kinetic energy ($\overline{\text{CEKE}}$) versus mean eddy kinetic energy ($\overline{\text{EKE}}$); b) Time-series of the coherent eddy number and the average coherent eddy amplitude; c) Map of the number of eddies; d) Map of the average coherent eddy amplitude; Seasonal cycle of the e) number of eddies, f) positive coherent eddy amplitude, and g) negative coherent eddy amplitude. Different lines represent the same as in Figure 9.

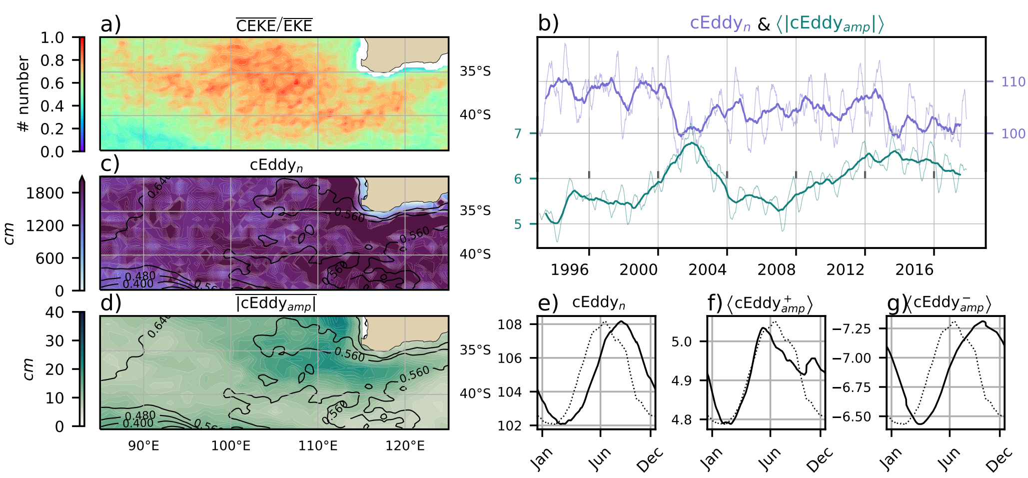

Figure 12. Climatology of the eddy field and coherent eddy field at the Leeuwin Current. a) Ratio of mean coherent eddy kinetic energy ($\overline{\text{CEKE}}$) versus mean eddy kinetic energy ($\overline{\text{EKE}}$); b) Time-series of the coherent eddy number and the average coherent eddy amplitude; c) Map of the number of eddies; d) Map of the average coherent eddy amplitude; Seasonal cycle of the e) number of eddies, f) positive coherent eddy amplitude, and g) negative coherent eddy amplitude. Different lines represent the same as in Figure 9.

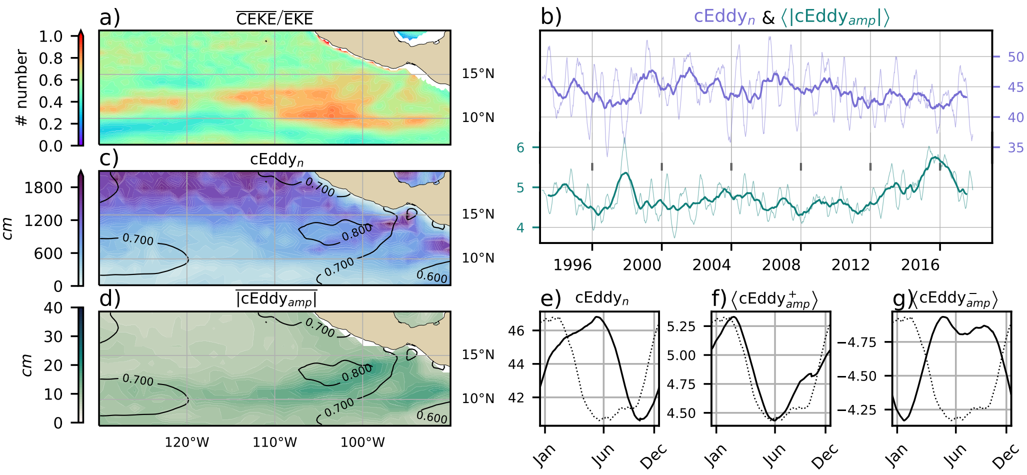

Figure 13. Climatology of the eddy field and coherent eddy field at the East Tropical Pacific. a) Ratio of mean coherent eddy kinetic energy ($\overline{\text{CEKE}}$) versus mean eddy kinetic energy ($\overline{\text{EKE}}$); b) Time-series of the coherent eddy number and the average coherent eddy amplitude; c) Map of the number of eddies; d) Map of the average coherent eddy amplitude; Seasonal cycle of the e) number of eddies, f) positive coherent eddy amplitude, and g) negative coherent eddy amplitude. Different lines represent the same as in Figure 9.

Another region with important contributions of the coherent eddy field is the East Tropical Pacific (Tehuantepec region; Figure 13), where coherent eddies contain ~58% of the energy. In fact, coherent eddy generation in this region is modulated by winds and coastlly trapped waves which produce a strong horizontal and vertical shear (baroclinic and barotropic instabilities; Zamudio et al., 2006). Furthermore, the equatorial generated waves propagating along the coast have an important interannual variability observable in the $\langle|\text{cEddy}_{amp}|\rangle$ time-series, where El Niño events are notable during 1997 and 2015 (Figure 13b). The seasonal cycle of cEddy$_n$, $\langle\text{cEddy}^+_{amp}\rangle$, and $\langle\text{cEddy}^-_{amp}\rangle$ support the idea of a coherent eddies responding to two different coherent eddy generation mechanisms; the number of eddies seasonal cycle lags for by ~3 months from the winds, while the $\langle\text{cEddy}^+_{amp}\rangle$ is on phase with the winds and the maximum of trapped waves (winter; Zamudio et al., 2006), and the $\langle\text{cEddy}^-_{amp}\rangle$ could be a consequence of eddy-eddy interactions.

7 Discussion and Conclusions

We investigated the contribution of coherent eddies in the kinetic energy field using satellite observations. We corroborate that around half of the EKE is explained by coherent eddies. This half is concentrated in eddy-rich regions where an intensification of the eddy field has been observed (Martínez-Moreno et al., 2021). The energy contained by eddies is larger than the previous estimate of 40% by Chelton et al. (2011). Although there are difference in the identification criteria of both eddy identification methods, the main cause of the difference is believed to be the lifespan and amplitude filters. These filters are widely used to track individual eddies on space and time, however, interactions between eddies in energetic regions my obscure the abundance and influence of short-lived coherent eddies. Filters are not used in this study, and indeed a lack of filters could facilitates an under or over-estimation of the the energy contained by coherent eddies, when miss-identifying or miss-fitting a coherent eddy. Thus, the presented estimate represents an upper limit of the energy contained by coherent eddies.

In addition, it should be noted that regions with first baroclinic Rossby radius of deformation smaller than 10km cannot be resolved by satellite observations. Thus, the energy contained by coherent eddies around latitudes of 60° and those near the shore are missed from this estimate, and remains unknown their role in the seasonal cycle and local dynamics. New satellite altimeter missions (SWOT) may allow to estimate energy contained by mesoscale coherent eddies outside the tropical region and the continental slope.

Hemispherical variability indicates a strong seasonal cycle of the EKE, CEKE, and eddy properties. The seasonal cycle of the CEKE in each hemisphere occurs as a consequence of numerous small coherent eddies interacting with each other (eddy-eddy interactions) and resulting in stronger, larger and more energetic coherent eddies during summer after a few months of the yearly coherent eddy number maxima. This results reveals eddy-eddy interactions and thus the transfer of energy from smaller coherent eddies to larger coherent eddies could explain the observed seasonal cycle of CEKE and coherent eddies properties.

Coherent eddy properties showcase a non-uniform long-term readjustment of the mesoscale eddy field. Overall, the eddy number has decreased globally at a significant rate of ∼35 eddies per decade from ∼4000 eddies identified globally on average each day.

However, large proportions of the ocean show an strengthening of the mesoscale coherent eddy field at a rate greater than ∼1 cm per decade. This strengthening of the coherent eddy amplitude is attributed to an intensification of each coherent eddy polarity, rather than a readjustment of the coherent eddy field to sea level rise. In other words, the coherent eddy amplitude intensification is occurring in both coherent eddy polarities and explain a proportion of the previously observed readjustments in the eddy field to long-term changes in the ocean forcing (Hu et al., 2020; Wunsch, 2020; Martínez-Moreno et al., 2021). This long-term readjustment showcases an intensification of the coherent eddy field, possibly due to long-term readjustments in the ocean baroclinic and barotropic instabilities, as well as the strength of the winds.

The reconstruction of the coherent eddies and their statistics have revealed regions with important coherent eddy contributions and a distinct seasonal evolution of the coherent eddies. Remarkably, western boundary extensions generate eddies through the instability of the main currents and the seasonal cycle of coherent eddies, CEKE, and thus EKE could be associated with an inverse energy cascade observable through lagged seasonal cycles in the coherent eddy statistics. In addition to this, the amplitude of the seasonal cycle in the boundary extensions is two times larger than any other region, thus the seasonality of the coherent eddies in boundary extensions dominate the hemispherical seasonal cycle. Furthermore, the seasonal lag of the inverse energy cascade is coupled with the presence of fronts, such is the case of western boundary extensions, and our results are consistent with the notion of baroclinic instability generating eddies and through eddy-eddy interactions an lagged inverse energy cascade.

The use of satellite observations in this study limit our ability to quantify the importance of the inverse energy cascade seasonality in the control of the coherent eddy seasonal cycle. As mentioned above, there is robust evidence of an increase in eddy-eddy interactions, however we can not discard important contributions from other processes such as the seasonal cycle of forcing and instabilities, which are crucial in the generation of coherent eddies. Although this study can provide a descriptive response of the coherent eddy field, further studies are needed to asses the role of eddy-eddy interactions in our changing climate, ocean dynamics, and biogeochemical process. Furthermore, the SWOT mission could allow to advance our understanding of eddy-eddy interactions and the seasonal cycle of scales smaller than mesoscale, which may provide further evidence of the inverse energy cascade driving the coherent eddy seasonality.

Acknowledgments

Chelton & Schlax (2013) dataset was produced by SSALTO/DUACS and distributed by AVISO+ (https://www.aviso.altimetry.fr/) with support from CNES, developed and validated in collaboration with E.Mason at IMEDEA. Global coherent eddy reconstruction, coherent and non-conherent eddy kinetic energy datasets, in addition to gridded coherent eddy tracking datasets are publicly available at (https://doi.org/10.5281/zenodo.4646429). All analyses and figures in this manuscript are reproducible via Jupyter notebooks and instructions can be found in the Github repository CEKE_climatology (https://github.com/josuemtzmo/CEKE_climatology). Trends used the Python Package xarrayMannKendall (https://doi.org/10.5281/zenodo.4458776)

References

Arbic, B. K., Polzin, K. L., Scott, R. B., Richman, J. G., & Shriver, J. F. (2013). On Eddy Viscosity, Energy Cascades, and the Horizontal Resolution of Gridded Satellite Altimeter Products*. *Journal of Physical Oceanography*, *43*(2), 283–300. doi: 10.1175/jpo-d-11-0240.1

Ashkezari, M. D., Hill, C. N., Follett, C. N., Forget, G., & Follows, M. J. (2016). Oceanic eddy detection and lifetime forecast using machine learning methods. *Geophysical Research Letters*, *43*(23). doi: 10.1002/2016gl071269

Beron-Vera, F. J., Wang, Y., Olascoaga, M. J., Goni, G. J., & Haller, G. (2013). Objective Detection of Oceanic Eddies and the Agulhas Leakage. *Journal of Physical Oceanography*, *43*(7), 1426–1438. doi: 10.1175/JPO-D-12-0171.1

Bouali, M., Sato, O. T., & Polito, P. S. (2017). Temporal trends in sea surface temperature gradients in the South Atlantic Ocean. *Remote Sensing of Environment*, *194*, 100–114. doi: 10.1016/j.rse.2017.03.008

Callies, J., Flierl, G., Ferrari, R., & Fox-Kemper, B. (2015). The role of mixed-layer instabilities in submesoscale turbulence. *Journal of Fluid Mechanics*, *788*, 5–41. doi: 10.1017/jfm.2015.700

Cane, M. A., Clement, A. C., Kaplan, A., Kushnir, Y., Pozdnyakov, D., Seager, R., ... Murtugudde, R. (1997). Twentieth-Century Sea Surface Temperature Trends. *Science*, *275*(5302), 957–960. doi: 10.1126/science.275.5302.957

Chaudhuri, A. H., Gangopadhyay, A., & Bisagni, J. J. (2009). Interannual variability of Gulf Stream warm-core rings in response to the North Atlantic Oscillation.

Continental Shelf Research, *29*(7), 856–869. doi: 10.1016/j.csr.2009.01.008

Chelton, D. B., A, d. R., Schlax, M. G., Naggar, K., & Siwertz, N. (1998). Geographical variability of the first baroclinic Rossby radius of deformation. *Journal of Physical Oceanography*, *28*(3), 433-460. doi: 10.1175/1520-0485(1998)028⟨0433:GVOTFB⟩2.0.CO;2

Chelton, D. B., Gaube, P., Schlax, M. G., Early, J. J., & Samelson, R. M. (2011). The influence of nonlinear mesoscale eddies on near-surface oceanic chlorophyll. *Science*, *334*(6054), 328-32. doi: 10.1126/science.1208897

Chelton, D. B., & Schlax, M. G. (2013). *Mesoscale eddies in altimeter observations of ssh.*

Chelton, D. B., Schlax, M. G., Samelson, R. M., & de Szoeke, R. A. (2007). Global observations of large oceanic eddies. *Geophysical Research Letters*, *34*(15), L15606. doi: 10.1029/2007GL030812

CMEMS. (2017). The Ssalto/Duacs altimeter products were produced and distributed by the Copernicus Marine and Environment Monitoring Service. *Aviso Dataset*. Retrieved from https://www.aviso.altimetry.fr/

Cui, W., Wang, W., Zhang, J., & Yang, J. (2020). Identification and census statistics of multicore eddies based on sea surface height data in global oceans. *Acta Oceanologica Sinica*, *39*(1), 41–51. doi: 10.1007/s13131-019-1519-y

Faghmous, J. H., Frenger, I., Yao, Y., Warmka, R., Lindell, A., & Kumar, V. (2015, 6). A daily global mesoscale ocean eddy dataset from satellite altimetry. *Scientific Data*, *2*, 150028 EP -. doi: 10.1038/sdata.2015.28

Ferrari, R., & Wunsch, C. (2009). Ocean Circulation Kinetic Energy: Reservoirs, Sources, and Sinks. *Annual Review of Fluid Mechanics*, *41*(1), 253–282. doi: 10.1146/annurev.fluid.40.111406.102139

Frenger, I., Gruber, N., Knutti, R., & Münnich, M. (2013). Imprint of Southern Ocean eddies on winds, clouds and rainfall. *Nature Geoscience*, *6*(8), 608 EP -. doi: 10.1038/ngeo1863

Frenger, I., Münnich, M., Gruber, N., & Knutti, R. (2015). Southern Ocean eddy phenomenology. *Journal of Geophysical Research: Oceans*, *120*(11), 7413-7449. doi: 10.1002/2015JC011047

Fu, L., Chelton, D., Le Traon, P., & Oceanography, M. R. (2010). Eddy dynamics from satellite altimetry. *Oceanography*, *23*(4), 14-25. doi: 10.2307/24860859

Gill, A., Green, J., & Simmons, A. (1974). Energy partition in the large-scale ocean circulation and the production of mid-ocean eddies. *Deep Sea Res Oceanogr Abstr*, *21*(7), 499-528. doi: 10.1016/0011-7471(74)90010-2

Hogg, A. M., & Blundell, J. R. (2006). Interdecadal variability of the southern ocean. *Journal of Physical Oceanography*, *36*(8), 1626-1645. doi: 10.1175/JPO2934.1

Hogg, A. M., Meredith, M. P., Chambers, D. P., Abrahamsen, E. P., Hughes, C. W., & Morrison, A. K. (2015). Recent trends in the Southern Ocean eddy field. *Journal of Geophysical Research: Oceans*, *120*(1), 257-267. doi: 10.1002/2014JC010470

Hu, S., Sprintall, J., Guan, C., McPhaden, M. J., Wang, F., Hu, D., & Cai, W. (2020, 2). Deep-reaching acceleration of global mean ocean circulation over the past two decades. *Science Advances*, *6*(6), eaax7727. doi: 10.1126/sciadv.aax7727

Japan Meteorological Agency, Japan. (2013). *Jra-55: Japanese 55-year reanalysis, daily 3-hourly and 6-hourly data.* Boulder CO: Research Data Archive at the National Center for Atmospheric Research, Computational and Information Systems Laboratory. Retrieved from `https://doi.org/10.5065/D6HH6H41`

Kang, D., & Curchitser, E. N. (2013). Gulf stream eddy characteristics in a high-resolution ocean model. *Journal of Geophysical Research: Oceans*, *118*(9), 4474-4487. Retrieved from `https://agupubs.onlinelibrary.wiley.com/doi/abs/10.1002/jgrc.20318` doi: https://doi.org/10.1002/jgrc.20318

Kang, D., & Curchitser, E. N. (2017). On the Evaluation of Seasonal Variability of the Ocean Kinetic Energy. *Geophysical Research Letters*, *47*, 1675-1583. doi: 10.1175/JPO-D-17-0063.1

Li, G., Cheng, L., Zhu, J., Trenberth, K. E., Mann, M. E., & Abraham, J. P. (2020). Increasing ocean stratification over the past half-century. *Nature Climate Change*, 1–8. doi: 10.1038/s41558-020-00918-2

Martínez-Moreno, J., Hogg, A. M., England, M., Constantinou, N. C., Kiss, A. E., & Morrison, A. K. (2021). Global changes in oceanic mesoscale currents over the satellite altimetry record. *Journal of Advances in Modeling Earth Systems*, *0*(ja). doi: 10.1029/2019MS001769

Martínez-Moreno, J., Hogg, A. M., Kiss, A. E., Constantinou, N. C., & Morrison,

A. K. (2019). Kinetic energy of eddy-like features from sea surface altimetry. *Journal of Advances in Modeling Earth Systems*, *11*(10), 3090-3105. doi: 10.1029/2019MS001769

Patel, R. S., Llort, J., Strutton, P. G., Phillips, H. E., Moreau, S., Pardo, P. C., & Lenton, A. (2020). The Biogeochemical Structure of Southern Ocean Mesoscale Eddies. *Journal of Geophysical Research: Oceans*, *125*(8). doi: 10.1029/2020jc016115

Pilo, G. S., Mata, M. M., & Azevedo, J. L. L. (2015). Eddy surface properties and propagation at Southern Hemisphere western boundary current systems. *Ocean Science*, *11*(4), 629–641. doi: 10.5194/os-11-629-2015

Qiu, B. (1999). Seasonal Eddy Field Modulation of the North Pacific Subtropical Countercurrent: TOPEX/Poseidon Observations and Theory. *Journal of Physical Oceanography*, *29*(10), 2471–2486. doi: 10.1175/1520-0485(1999)029⟨2471:sefmot⟩2.0.co;2

Qiu, B., & Chen, S. (2004). Seasonal Modulations in the Eddy Field of the South Pacific Ocean. *Journal of Physical Oceanography*, *34*(7), 1515–1527. doi: 10.1175/1520-0485(2004)034⟨1515:smitef⟩2.0.co;2

Qiu, B., Chen, S., Klein, P., Sasaki, H., & Sasai, Y. (2014). Seasonal Mesoscale and Submesoscale Eddy Variability along the North Pacific Subtropical Countercurrent. *Journal of Physical Oceanography*, *44*(12), 3079–3098. doi: 10.1175/JPO-D-14-0071.1

Ruela, R., Sousa, M. C., deCastro, M., & Dias, J. M. (2020). Global and regional evolution of sea surface temperature under climate change. *Global and Planetary Change*, *190*, 103190. doi: 10.1016/j.gloplacha.2020.103190

Sasaki, H., Klein, P., Qiu, B., & Sasai, Y. (2014). Impact of oceanic-scale interactions on the seasonal modulation of ocean dynamics by the atmosphere. *Nature Communications*, *5*(1), 5636. doi: 10.1038/ncomms6636

Schubert, R., Schwarzkopf, F. U., Baschek, B., & Biastoch, A. (2019). Submesoscale Impacts on Mesoscale Agulhas Dynamics. *Journal of Advances in Modeling Earth Systems*, *11*(8), 2745–2767. doi: 10.1029/2019ms001724

Siegel, D., Peterson, P., DJ, M., Maritorena, S., & Nelson, N. (2011). Bio-optical footprints created by mesoscale eddies in the Sargasso Sea. *Geophysical Research Letters*, *38*(13), n/a-n/a. doi: 10.1029/2011GL047660

Uchida, T., Abernathey, R., & Smith, S. (2017). Seasonality of eddy kinetic energy in an eddy permitting global climate model. *Ocean Modelling*, *118*, 41-58. doi: 10.1016/j.ocemod.2017.08.006

Wunsch, C. (2020). Is The Ocean Speeding Up? Ocean Surface Energy Trends. *Journal of Physical Oceanography*, *50*(11), 1–45. doi: 10.1175/jpo-d-20-0082.1

Wunsch, C., & Ferrari, R. (2004). Vertical mixing, energy, and the general circulation of the oceans. *Annual Review of Fluid Mechanics*, *36*(1), 281–314. doi: 10.1146/annurev.fluid.36.050802.122121

Wyrtki, K., Magaard, L., & Hager, J. (1976). Eddy energy in the oceans. *Journal of Geophysical Research*, *81*(15), 2641-2646. doi: 10.1029/JC081i015p02641

Yue, S., & Wang, C. (2004). The Mann-Kendall Test Modified by Effective Sample Size to Detect Trend in Serially Correlated Hydrological Series. *Water Resources Management*, *18*(3), 201–218. doi: 10.1023/b:warm.0000043140.61082.60

Zamudio, L., Hurlburt, H. E., Metzger, E. J., Morey, S. L., O'Brien, J. J., Tilburg, C., & Zavala-Hidalgo, J. (2006). Interannual variability of Tehuantepec eddies. *Journal of Geophysical Research: Oceans (1978–2012)*, *111*(C5). doi: 10.1029/2005JC003182